Radiation Measurements 189 (2025) 107538

Contents lists available at ScienceDirect

Radiation Measurements

journal homepage: www.elsevier.com/locate/radmeas

Utilizing the coincidence and anti-coincidence counting of crosstalk events to enhance measurement accuracy in BNCT-SPECT

Yu Fujiwara, Mana Miyagawa, Mikito Yagura, Jiye Qiu, Shingo Tamaki, Sachie Kusaka, Fuminobu Sato, Isao Murata *

Division of Sustainable Energy and Environmental Engineering, Graduate School of Engineering, The University of Osaka, Yamada-oka 2-1, Suita, Osaka, 565-0871, Japan

ARTICLE INFO

Keywords:
Medical diagnostics and therapy
Boron neutron capture therapy
GAGG scintillator
Single photon emission computed tomography
Crosstalk

ABSTRACT

Single Photon Emission Computed Tomography (SPECT) in Boron Neutron Capture Therapy (BNCT) plays a vital role in real-time monitoring of treatment effects. However, image quality can be degraded by background noise. We propose a novel noise-reduction technique that utilizes both coincidence and anti-coincidence counting methods, leveraging the crosstalk phenomenon between adjacent scintillators. To evaluate the feasibility of this approach, we measured γ-ray spectra from a ^{137}Cs standard source using two GAGG scintillators. The results showed noise reduction improvements of 15.9 % with coincidence and 3.8 % with anti-coincidence methods. Additionally, theoretical analysis demonstrated that this approach is effective in multiple scintillators arranged by the forward nature of Compton Scattering. This approach offers a promising path toward improving BNCT-SPECT imaging quality by effectively discriminating target signals from noise in high-density detector arrays.

1. Introduction

Boron Neutron Capture Therapy (BNCT) is a promising radiotherapy for cancers, which allows selective treatment of the tumor cells with little damage (Locher, 1936). BNCT administers boron drugs to cancer cells, and epi-thermal neutrons (0.5 eV–10 keV) are irradiated to patients. Neutrons slow down to thermal neutrons through the body, and ^{7}Li and alpha particles from ^{10}B (n, α) ^{7}Li reactions damage tumor cells. Since the ranges of these particles are within 10 μm, almost the same as the diameter of a single cell, healthy cells are spared (Sauerwein et al., 2012).

Since BNCT employs high doses of epi-thermal neutrons, monitoring boron concentrations within the body is crucial to assess the treatment effect (International Atomic Energy Agency, 2023). Due to the dynamic nature of boron distribution, real-time verification is preferred over indirect methods such as Inductively Coupled Plasma and Positron Emission Tomography (Ishiwata, 2019; Linko et al., 2008). To achieve this objective, different systems were proposed to image boron spatial distribution by measuring the 478 keV prompt γ-rays emitted from Boron-neutron capture reactions expressed as

$$^{10}B + n \rightarrow {}^{7}Li + \alpha + 2.79\ MeV\ (6.3\%) \rightarrow {}^{7}Li^{*} + \alpha + 2.31\ MeV\ (93.7\%) \quad (1)$$

$$^{7}Li^{*} \rightarrow {}^{7}Li + \gamma\ (478\ keV) \quad (2)$$

The intensity of 478 keV γ-rays is proportional to the boron local dose. Nowadays, the single-photon emission tomography (SPECT) technique (Caracciolo et al., 2024; Hales et al., 2017; Ishikawa et al., 2001; Kim et al., 2021; Kobayashi et al., 2000; Murata et al., 2022; Winkler et al., 2017), Compton cameras (Qiu et al., 2025; Sakai et al., 2023) are being developed for real-time verification of the treatment effect in BNCT. We also focused on the BNCT-SPECT system and have developed a design based on the gadolinium aluminum gallium garnet, $Gd_3Al_2Ga_3O_{12}$: Ce (GAGG (Ce)) scintillators (Murata et al., 2022). SPECT measures the prompt γ-rays emitted in equation (2), and the collimated array detector detects the γ-rays as shown in Fig. 1. We deduced a three-dimensional distribution regarding the prompt γ-rays from the result, leading to the boron dose distribution.

Previous studies have performed the design investigation of BNCT-SPECT, including the composition of the detector and collimator (Caracciolo et al., 2024; Hales et al., 2017; Ishikawa et al., 2001;

This article is part of a special issue entitled: Scintillators Applications published in Radiation Measurements.

* Corresponding author.
E-mail address: murata@see.eng.osaka-u.ac.jp (I. Murata).

https://doi.org/10.1016/j.radmeas.2025.107538
Received 22 May 2025; Received in revised form 18 September 2025; Accepted 9 October 2025
Available online 14 October 2025

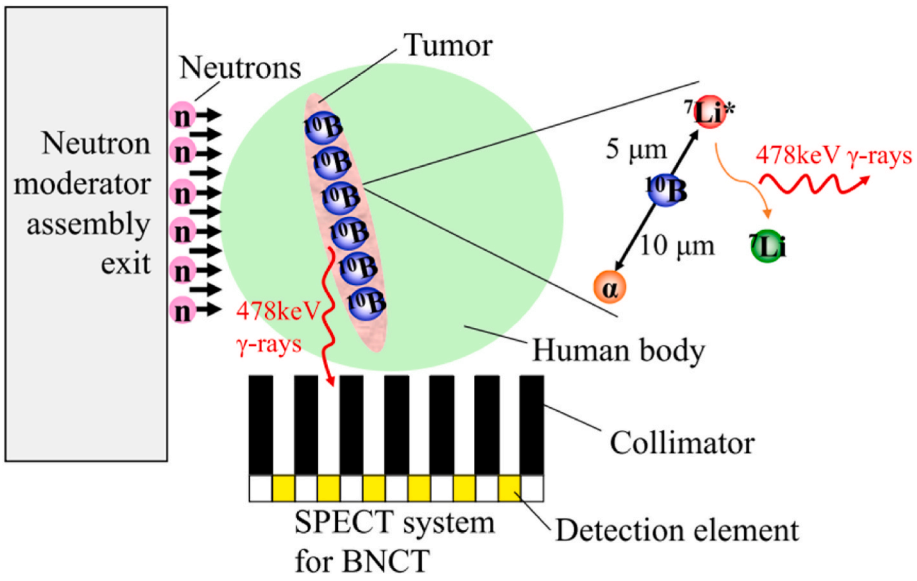

Fig. 1. Conceptual illustration of BNCT-SPECT (Figure was extracted from ref (Murata et al., 2022). Neutrons are emitted from the Neutron moderator assembly and reach the human body. Patients are close to the wall. BNCT-SPECT is set-up also close to the patient to avoid the neutron beam direction.

Table 1
Design examples of BNCT-SPECT.

Resource	Detector		Collimator			Spatial Resolution
	Material	Size	Material	Hole size (mm)	Length (cm)	
Kobayashi et al. (2000)	CdTe	(No Stated, NS)	Tungsten	4 × 4	20	1 cm
Ishikawa et al. (2001)	BGO	5 cm × 5 mm φ	Heavy Metal	5.4 φ	32.1	1 cm
Minsky et al. (2011)	$LaBr_3$	1 inch × 1 inch φ	Lead	5 φ	30	10 mm
Hales et al. (2017)	CZT	1 cm × 1 cm × 1 cm	Lead	4 × 4	20	10 mm
Murata et al. (2022)	GAGG	3.5 mm × 3.5 mm × 30 mm	Tungsten	3.5 φ	26	5.1 mm
Caracciolo et al., (2024)	$LaBr_3$	5 cm × 5 cm × 2 cm	Lead	NS	10	8 mm

Kobayashi et al., 2000; Minsky et al., 2011; Murata et al., 2022). Table 1 presents the design results; our BNCT-SPECT system had a high spatial resolution that enabled us to distinguish the tumor, compared to the other studies (Murata et al., 2022). However, the issue of signal discrimination remains because the neutron source of BNCT is extremely intense; for instance, IAEA suggested that the neutron intensity was greater than $5 \times 10^8\ (n/cm^2/sec)$ (International Atomic Energy Agency, 2023), thereby including many background counts around the 478 keV peak in the pulse height spectra (PHS). Typical examples are the Compton continuum of 2.22 MeV γ-rays emitted by the ^{1}H (n, γ) ^{2}H reaction, annihilation γ-rays of 511 keV created via the annihilation reaction of positrons produced by the electron creation reaction of γ-ray or emitted electron via β^+ decay of radioisotopes produced by neutron interaction, and so on. Therefore, the detector inevitably requires an appropriate energy resolution to separate 478 keV and 511 keV γ-rays. At least our previous study didn't correct such effects; this contribution should affect the performance of the imaging quality.

In order to improve the measurement accuracy of 478 keV γ-rays, we propose a novel approach leveraging the crosstalk phenomenon. When several scintillators are placed close together, signals from the deposited γ rays are detected simultaneously in several elements due to Compton scattering. Crosstalk obviously occurs in the BNCT-SPECT system, where we have used 8 × 8 array-type GAGG scintillators (3.5 × 3.5 × 30 mm^3) at 4 mm intervals. Traditionally, crosstalk has been considered a source of background noise (Du and Frey, 2009), and several methods have been developed to mitigate signals arising from this phenomenon (Rosado and Hidalgo, 2015; Sakai et al., 2020; Trigila et al., 2024; Tsartsalis et al., 2018). Monte Carlo simulations have been used to evaluate the contributions of crosstalk (Rosado and Hidalgo, 2015; Trigila et al., 2024), but eliminating this effect remains challenging. The Dual-Energy Window (DEW) approach combines two images generated from high- and low-energy radiation sources to reduce this effect. (Sakai et al., 2020; Tsartsalis et al., 2018). However, detailed corrections are required for images derived from lower-energy radiation.

The crosstalk phenomenon has the potential to be utilized to improving measurement accuracy through the combination of coincidence counting and anti-coincidence counting. Coincidence counting detects the signal provided that several pulses enter the detector at the same time. If the sum energy of these signals is 478 keV, adding this sum peak helps to increase the count. On the other hand, if the sum is not 478 keV, removing them will reduce the background noise. Previous studies have shown the effectiveness of either the coincidence method (Uenomachi et al., 2022) or the anti-coincidence counting method (Manabe et al., 2016; Miyamaru et al., 2025). However, our proposed approach has the significant advantage of simultaneously applying both coincidence and anti-coincidence events to improve measurement accuracy.

In the first step of this noise reduction approach, this study aimed to validate this approach using a ^{137}Cs standard radiation source with 2 scintillators. The experimental and simulation results demonstrated that the proposed method could significantly reduce the background noise, suggesting that this approach becomes a promising way to evaluate the

Table 2
Summary of scintillators' characteristics. Data was extracted from (Brown, 2023; Glodo et al., 2005; Kamada et al., 2016; Mao et al., 2008; Moszynski et al., 1997).

Scintillators	GAGG (Ce)	NaI (TI)	CsI (TI)	$LaBr_3$	BGO
Density (g/cm^3)	6.63	3.67	4.51	5.08	7.13
Light yield (Photons/MeV)	56000	45000	56000	74000	8000
Energy resolution for the 662 keV ^{137}Cs γ-ray source (%)	6.3	5.6	5.7	2.6	12
hygroscopic	No	Yes	Yes	Yes	No

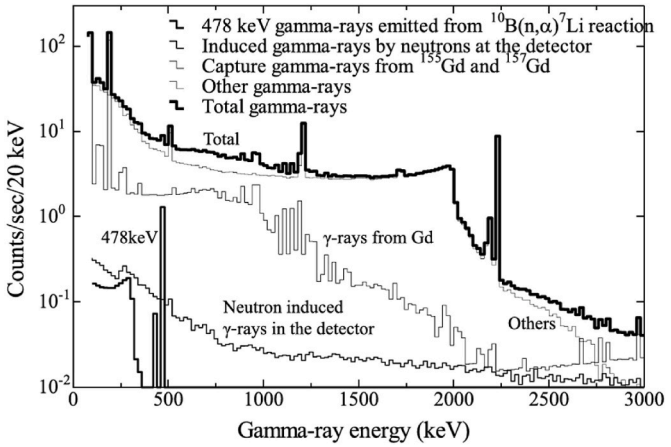

Fig. 2. Example of PHS to be measured by the GAGG scintillator, calculated in Monte Carlo N-particle code 5 (MCNP 5) with the conditions, i.e., GAGG scintillator dimensions of 3.5 × 3.5 × 30 mm, collimator hole diameter of 3 mm, and collimator length of 25 cm (Murata et al., 2022).

real-time treatment effect in BNCT.

2. Materials and methods

2.1. Design requirements of the GAGG-based BNCT-SPECT

This study adopted 8 × 8 array-type GAGG scintillators made by C&A Corporation Inc. For material selection, it is essential to consider density, light yield, and energy resolution. Table 2 presents these characteristics in each scintillator, highlighting the competitive performances of GAGG compared to other scintillators. GAGG has a high density compared to other scintillator materials such as NaI or CsI, i.e., and also has high energy and spatial resolution for the 662 keV ^{137}Cs γ-ray source (Kamada et al., 2016). $LaBr_3$ also exhibits high performance in these criteria; however, hygroscopic is a significant issue to address. Moreover, its inherent self-radioactivity poses another concern. The CdTe detector is one of the semiconductor detectors for which our research group had previously developed a BNCT-SPECT system based on (Manabe et al., 2016; Manabe et al., 2016; Murata et al., 2014). It also has outstanding performances in terms of energy resolution; however, due to a polarization problem and high cost, we applied GAGG scintillators instead.

In order to evaluate the monitoring performance in BNCT-SPECT, two goals were set (Murata et al., 2022).

I. Statistical accuracy of γ-rays from the ^{10}B (n, α) ^{7}Li reaction.

In addition to this reaction, several occurrence mechanisms exist in clinical BNCT. For example, neutron absorption by the gadolinium in GAGG or hydrogen in the human body, and the electron-positron annihilation, as shown in Fig. 2 (Goorley and Nikjoo, 2000). The

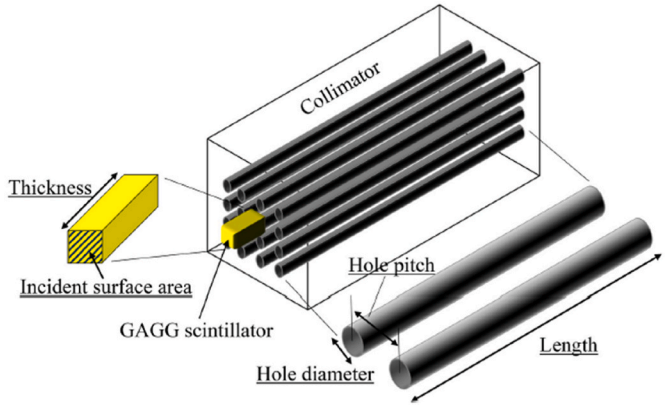

Fig. 3. Schematic Geometry to design our BNCT-SPECT system (Murata et al., 2022). Since this design work was performed for only one scintillator, it is not sufficient to reproduce the actual environment of the BNCT treatment. Background noise from several pathways, such as C_{Gd}, C_N, and C_γ, seems to affect the evaluation factor.

counting rate and standard deviation accounted for this parameter. Let N_{BNCT} and σ_{BNCT} be the counts and standard deviation of γ-rays from the ^{10}B (n, α) ^{7}Li reaction, and N_{BG} and σ_{BG} be those of background noise, and the statistical accuracy (A) was defined in the following equation (3).

$$A = \frac{\sigma_{BNCT}}{N_{BNCT}} \times 100 = \frac{\sqrt{{\sigma_{Total}}^2 + {\sigma_{BG}}^2}}{N_{BNCT}} \times 100, \quad (3)$$

Where σ_{Total} is the deviation of the γ-ray counts for all patterns generated in BNCT fields, and $\sigma_{BNCT} = \sqrt{{\sigma_{Total}}^2 + {\sigma_{BG}}^2}$. According to Fig. 2, these count rates are written in the following equations.

$$N_{BNCT} = C_B \quad (4)$$

$$N_{BG} = C_{Gd} + C_N + C_\gamma \quad (5)$$

$$N_{Total} = N_{BNCT} + N_{BG} = C_B + C_{Gd} + C_N + C_\gamma, \quad (6)$$

Where C_B is the counting rate of the ^{10}B (n, α) ^{7}Li reaction, C_{Gd} is the γ-rays produced by gadolinium neutron capture, C_N is the induced γ-rays from neutrons, and C_γ is other γ-rays. Therefore, A is given in the following Equation;

$$A = \frac{\sqrt{{\sigma_{Total}}^2 + {\sigma_{BG}}^2}}{N_{BNCT}} \times 100 = \frac{\sqrt{C_B + 2(C_{Gd} + C_N + C_\gamma)}}{C_B} \times 100 \quad (7)$$

II. Signal-to-Noise ratio (S/N ratio).

The S/N ratio accounts for the ratio of background noise to the target signals, as described in equation (8).

$$S/N = \frac{N_{BNCT}}{N_{BG}} = \frac{C_B}{C_{Gd} + C_N + C_\gamma} \quad (8)$$

From equations (3) to (8), background signal discrimination is important for the BNCT-SPECT system. Our system performed with high statistical accuracy (A = 4.4 % and S/N ratio = 0.15) (Minami et al., 2017) and also high spatial resolution, as displayed in Table 1. However, this analysis was based on the case of a single scintillator, as presented in Fig. 3. Since the actual system deploys 64 GAGG scintillators, the background noise effect should be higher. It also causes the crosstalk phenomenon elaborated in the following section 2.2, which enhances the effect of background noise.

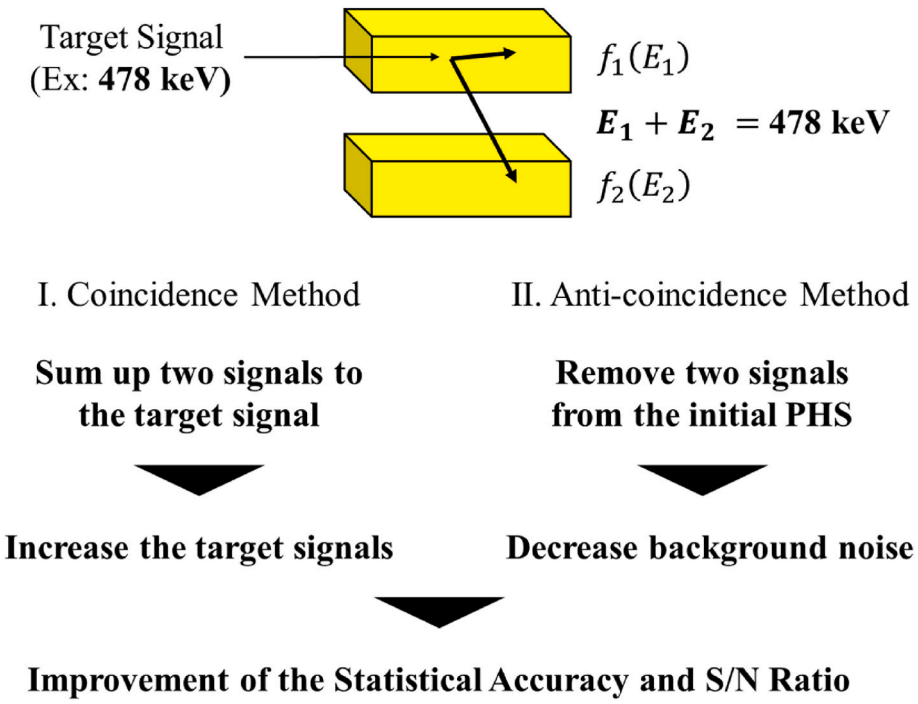

Fig. 4. Concept of Coincidence/Anti-Coincidence Methods. When the sum of the signals' energy in coincidence events is 478 keV, it is added to the target signals (coincidence method). On the other hand, since each signal is regarded as an error count, it is removed by the anti-coincidence method.

2.2. Methods for enhancing measurement accuracy

The crosstalk phenomenon happens when multiple scintillators are set close together. When γ-rays irradiate a GAGG scintillator, some of them cause Compton scattering, emitting electrons and scattered γ-rays simultaneously. If they are detected in another scintillator, such ionization radiation becomes noise. Since our proposed design of BNCT-SPECT employs small GAGG scintillators with narrow intervals, crosstalk phenomena cannot be ignored.

This study aims to reduce the counting noise using two discrimination methods, the coincidence/anti-coincidence counting method, by addressing the crosstalk phenomenon. Fig. 4 presents the principles of these approaches in the case of BNCT treatments. Note that this study adopted the ^{137}Cs source with a γ-ray energy of 662 keV, but the actual prompt γ-ray energy is 478 keV in BNCT treatments. The coincidence counting method adds coincidence events to the PHS in one scintillator if the sum of signals detected in each scintillator is 478 keV. On the other hand, the anti-coincidence counting method subtracts signals of the coincidence events from the PHS, if 478 keV γ-rays are also detected simultaneously at one scintillator. The coincidence method is employed to enhance the objective signals, 478 keV γ-rays emitted by the ^{10}B (n, α) ^{7}Li reaction (N_{BNCT} in Section 2.1), while the anti-coincidence method is used to reduce scattered background noise (N_{BG}). In this way, improvements in statistical accuracy and Signal-to-Noise ratio will be achieved.

Given $f_1(E)$ and $f_2(E)$ are the PHS for scintillator 1 and 2, they are written by the coincidence/anti-coincidence spectra below:

$$\begin{aligned} f_1(E) &= f_{1c}(E) + f_{1a}(E) \\ f_2(E) &= f_{2c}(E) + f_{2a}(E), \end{aligned} \tag{9}$$

Where $f_{1c}(E)$ and $f_{2c}(E)$ are the PHS in the coincidence events for each scintillator, and $f_{1a}(E)$ and $f_{2a}(E)$ are the ones in the anti-coincidence case.

Taking $f_{(1+2)c}(E)$ as the sum of the PHS in the coincidence events, equations (10) and (11) are valid.

$$\begin{aligned} f_c(E) &= f_1(E) + f_{(1+2)c}(E) - f_{1c}(E) \\ &= f_{1a}(E) + f_{(1+2)c}(E) \end{aligned} \tag{10}$$

$$f_a(E) = f_1(E) - f_{1c}(E) = f_{1a}(E) \tag{11}$$

In order to evaluate the effectiveness of the coincidence/anti-coincidence approach, the improvement rate (R) in the Peak-Compton ratio (P/C ratio) was applied. P/C ratio means the counting ratio of the photoelectronic peak and the Compton continuum, and R was described in the following equation (12).

$$R\ (\%) = \frac{P/C_{after} - P/C_{before}}{P/C_{before}} \times 100, \tag{12}$$

Where P/C_{before} is the P/C ratio before these noise reduction processes, and P/C_{after} is the one after them. It is a crucial factor in achieving the design goals of our BNCT-SPECT system. Since the improvement of the P/C ratio directly leads to the improvement of A and S/N ratio, this study pursued to enhance this parameter.

2.3. Experimental system

To demonstrate this approach, measurements for each scintillator, including coincidence events ($f_1(E)$, $f_2(E)$, and $f_c(E)$), were performed in an experimental system shown in Fig. 5. Fig. 5 (a) presents an overview of the experimental system. Lead and tungsten were installed as the collimator between the ^{137}Cs standard source and two GAGG scintillators, supported by an aluminum stand. One scintillator (S_1) was placed at the exit of the collimator hole to concentrate γ-rays on S_1 and to shield them from the other scintillator (S_2). This allows us to measure the contributions of the crosstalk phenomenon in S_2. The sketch of the collimator design is depicted in Fig. 5 (b). Scintillation light emitted from the GAGG scintillator was detected by the Multi-Pixel Photon Counter (MPPC) made by Hamamatsu Photonics Inc. (Photonics, 2017). The signals were amplified using the Silicon Photomultiplier and analyzed by the Multichannel Analyzer (MCA). The MCA enables the acquisition of the pulse height distribution from MPPC signals, which

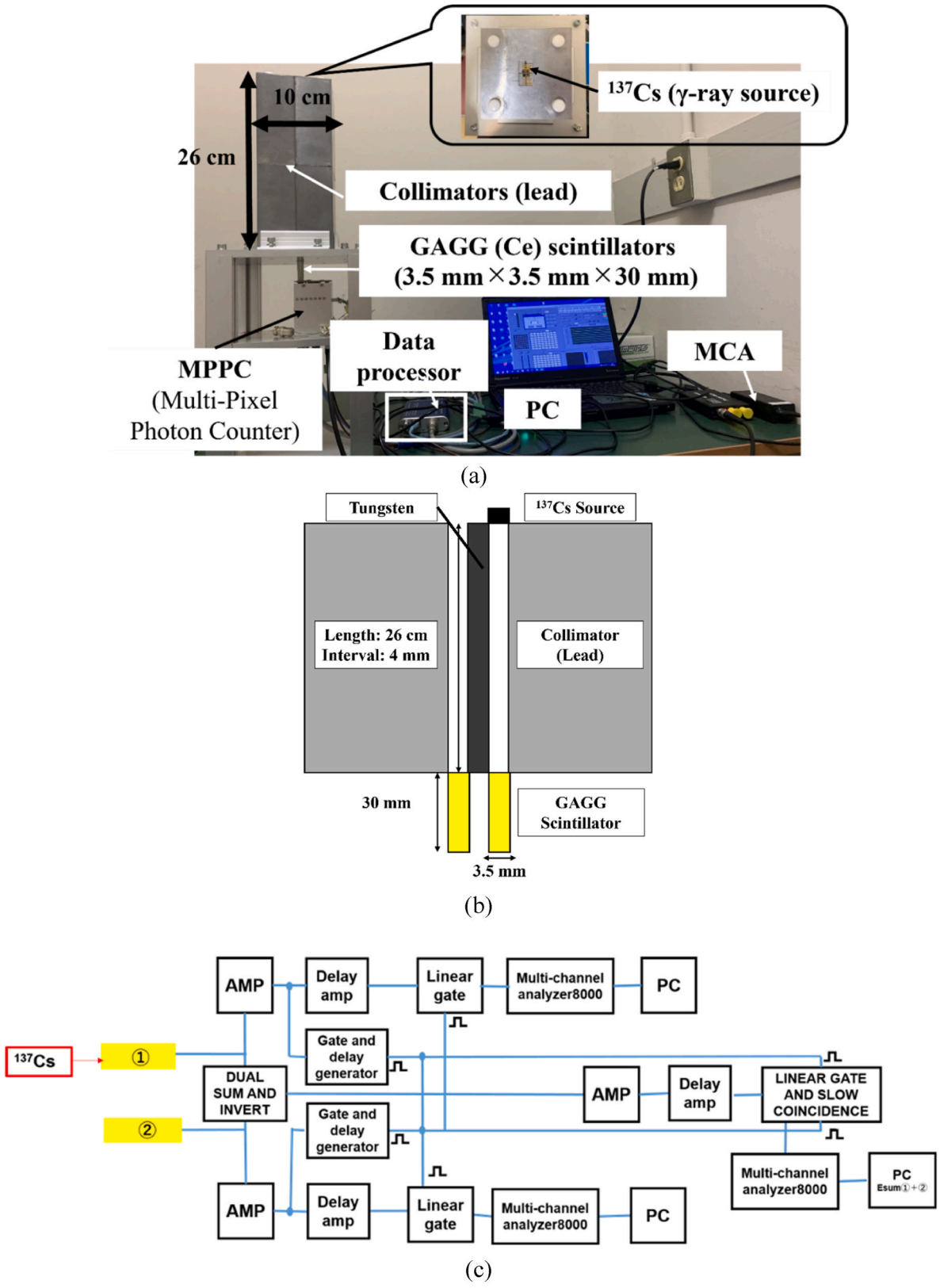

Fig. 5. (a) Overall experimental system. (b) A sketch of the ^{137}Cs source, collimator, and MPPC. (c) Schematic design of this circuit to measure coincidence events.

corresponds to voltage.

In order to measure signals of coincidence events, $f_c(E)$, several NIM modules were installed between the MPPC and MCA. Signals from the MPPC were amplified by the amplifiers (AMP, ORTEC 571). A delay amplifier (Delay amp, ORTEC 427A) was used to delay signals by 2 μs in this study for timing adjustment. The linear gate (ORTEC 426) plays a role in the gate for whether the signals pass through or not. By adjusting the time scale in the Gate and Delay Generator (ORTEC 416A) to ensure that gate signals reached the linear gate when input signals were introduced, a pulse height spectrum for coincidence events was ob-

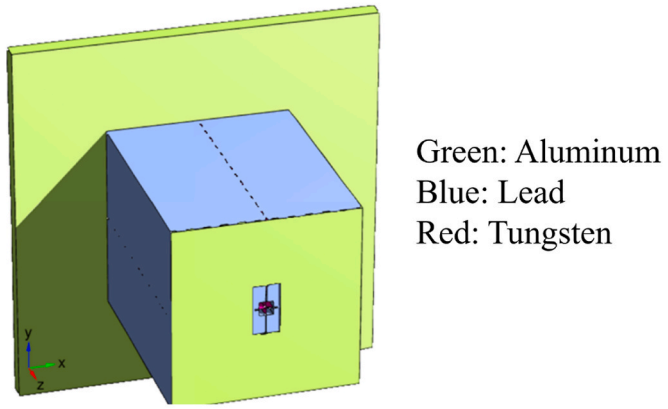

Fig. 6. Simulation Geometry in PHITS.

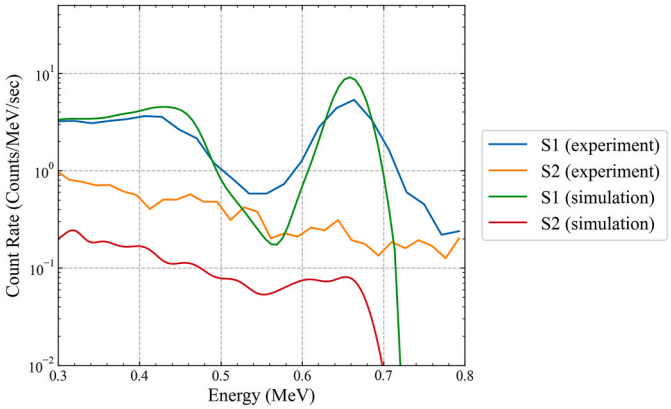

Fig. 7. PHS (f_1, f_2) in both the validation experiment and the [T-deposit] tally of PHITS.

tained. Moreover, a DUAL SUM AND INVERT (ORTEC 533) was also used to sum up signals in each scintillator. They were led to the LINEAR GATE AND SLOW COINCIDENCE (OKEN721-1), which generated gate signals if two logical signals were reached simultaneously. Therefore, a sum of PHS ($f_{(1+2)c}(E)$) for each scintillator in coincidence events by analyzed at the MCA.

The experimental system was set up, and after darkening the room to shield from ambient light, the PHS was measured for 2 h. A linear gate with a time window of 4 μs was applied, and the energy threshold was set to eliminate electrical background noise. Results were analyzed using the method described in Section 2.2, and R was evaluated.

2.4. Monte Carlo simulation

In this study, we modeled the experimental system in a Monte Carlo simulation code, PHITS (Sato et al., 2024) and compared the P/C ratio with that of the experimental result. The energy deposition in each scintillator was calculated in [T-deposit] tally. In addition, [T-deposit 2] tally was utilized to obtain the correlation of the energy deposition in the specified two regions; that is, it could determine the energy and its count when the crosstalk happens. Fig. 6 shows the simulation system in PHITS. The PHS obtained from the PHITS simulation was compared to the experimental results.

3. Results

3.1. Experimental results

Fig. 7 depicts the PHS of each scintillator in both the experimental and simulation results. A Gaussian distribution, obtained from the experimental results performed in the standard point sources, was incorporated into the simulation results to model the energy resolution of GAGG scintillators, and the unit was unified to [counts (/MeV/sec)] in order to compare the two. For S_1, a photoelectronic peak was measured at 662 keV, corresponding to the energy emitted by the ^{137}Cs source. Also, the escape peak appeared at 477 keV. On the other hand, there is no photoelectronic peak in S_2 because of the shielding by the collimator. The energy resolution was different from each other; however, the integral of peak counts in S_1 is 61.0, 64.42 (/sec), respectively, thereby the relative error is 5.3 %. Therefore, we regarded that the simulation results were successfully benchmarked by the experiment.

Fig. 8 (a) illustrates the PHS for coincidence events, which were extracted in Linear Gate and Slow Coincidence. Fig. 8 (b) shows the simulation result in [T-deposit 2] tally to evaluate the coincidence events. By taking the sum of values in the X-axis, PHS for the coincidence events in the S_1 can be defined, while the sum of values in the Y-axis represents the PHS of the S_2 (Red line and Blue line stand for $f_{1c}(400\,keV)$; $f_{2c}(400\,keV)$, respectively). $f_{(1+2)c}(E)$ was derived from counting the counts of X + Y = E (for instance, $f_{(1+2)c}(400\,keV)$ is obtained by summing the counts in the Green line). From the results of the coincidence events in Fig. 8 (a) and (c), peaks were observed around 450 keV for S_1 and 210 keV for S_2, respectively. That represented the peak in the sum of coincidental events ($f_{(1+2)c}(662\,keV)$). In addition, the simulation result in S_1 exhibits a peak at around 620 keV resulting from the photoelectric effect, while it didn't appear in the experimental result. In principle, all photons are absorbed when the photoelectric effect occurs; thus, nothing should be detected as the coincidence counts at this region. Except for this point, results clearly demonstrate that the crosstalk phenomenon enhances the count rate. The experimental result reproduced the simulation result, and the sum of each scintillator shows a peak at 662 keV. Therefore, this experiment demonstrated that [T-deposit 2] tally in PHITS can evaluate the behavior of the crosstalk phenomenon. In the following section, the analysis of the effect on the noise reduction is described based on the simulation results in PHITS.

3.2. Examination of the possibility noise reduction

Fig. 9 presents the PHS before and after the noise reduction approaches. "Raw data" refers to the simulation results of S_1, which represent the PHS prior to applying the coincidence or anti-coincidence methods. A clear improvement in Cp can be observed with the coincidence methods, while a slight reduction in C_C from anti-coincidence method is also evident. The results of the peak signal summation and the subtraction of the Compton signal, which is regarded as noise, using equations (9)–(11) are shown in Table 3. From the simulation result, P/C ratio was evaluated by equation (12). As the Compton edge was observed at 477 keV, the counts of the peak region C_P were obtained by calculating the sum of the counts in each energy bin over 477 keV, while the counts of the peak region C_C were obtained by taking the sum below 477 keV. Table 1 exhibits the Peak and Compton events counts and the P/C ratio in this study. R for each method (R_C, R_a) was also calculated in equation (12), as described below.

$$R_C = \frac{0.248 - 0.214}{0.214} \times 100 = 15.9\,\% \tag{13}$$

$$R_a = \frac{0.222 - 0.214}{0.214} \times 100 = 3.8\,\% \tag{14}$$

Therefore, the crosstalk phenomenon was found to contribute to noise reduction, and the coincidence method performed better than the

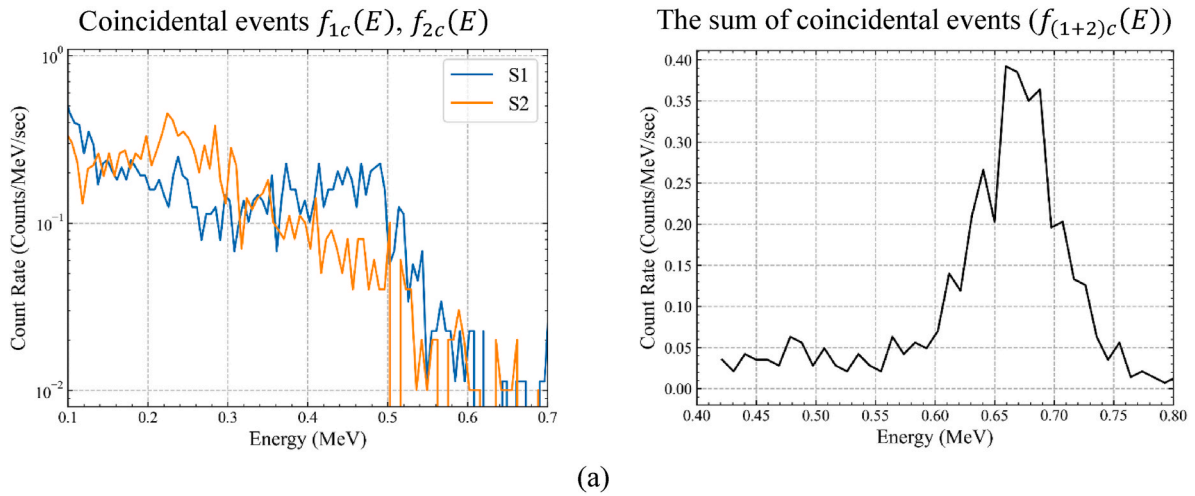

(a)

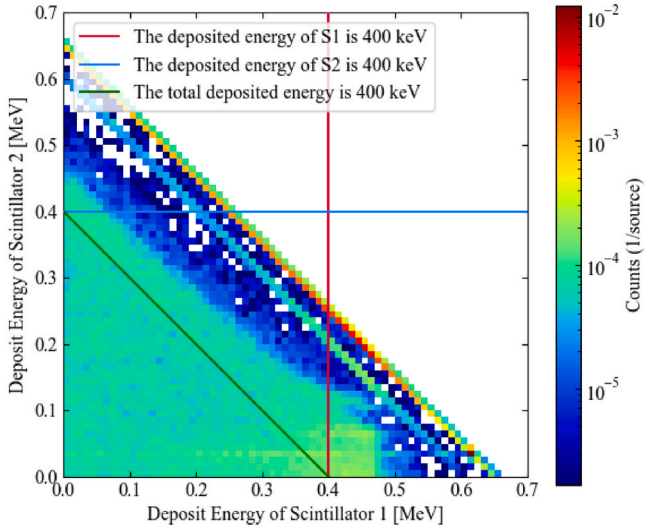

(b)

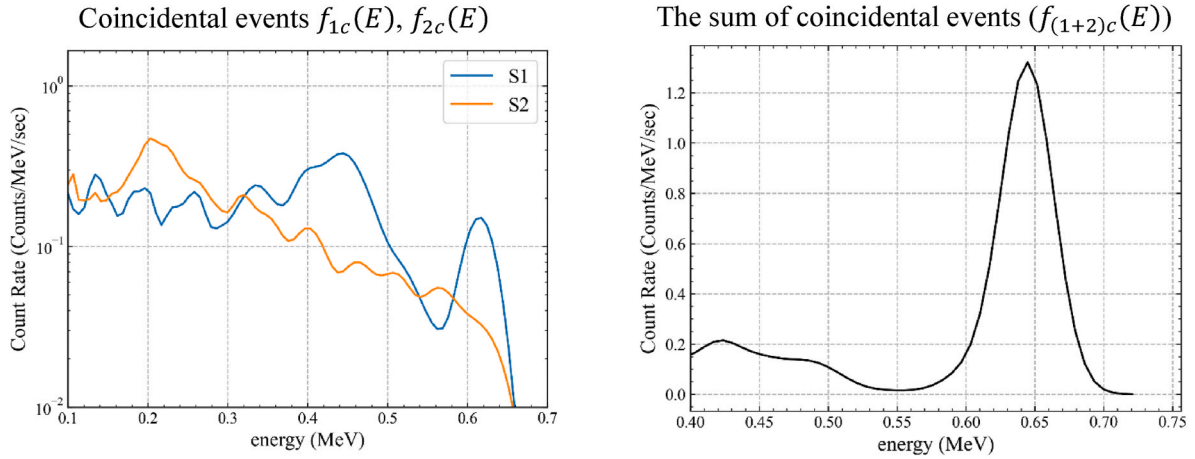

(c)

Fig. 8. (a) PHS for coincidence events in the validation experiment, (b) Image of the result in [T-deposit 2] tally. By counting signals in the blue line, the PHS of S_1 ($f_{1c}(E)$) was obtained. The PHS for the sum of coincidental events ($f_{(1+2)c}(E)$) was obtained by counting signals in the purple line. (c) PHS extracted from the [T-deposit 2] tally. (For interpretation of the references to color in this figure legend, the reader is referred to the Web version of this article.)

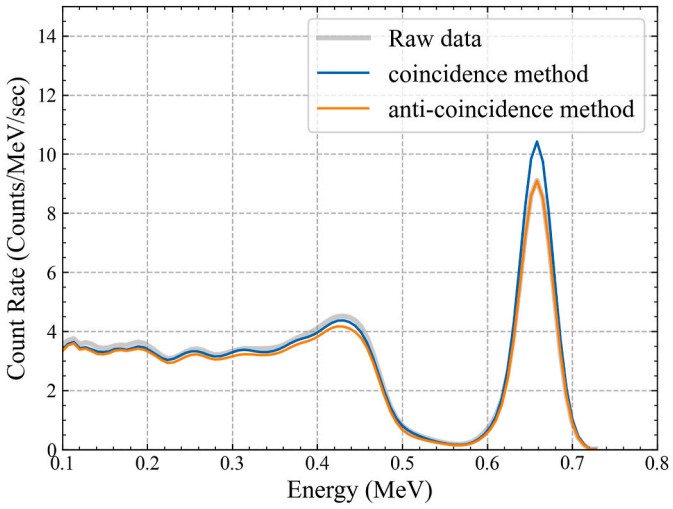

Fig. 9. PHS (f_1) before and after the noise reduction processes. This figure illustrates the increase of C_P by the coincidence method, and the reduction of C_C by the anti-coincidence method. PHS in "Raw data" is illustrated in grey, hidden by the PHS after the anti-coincidence method.

Table 3
Peak Compton Ratio extracted from the simulation result.

	Raw data	Coincidence method	Anti-coincidence method
C_P (Counts/MeV/sec)	69.1 ± 0.96	77.6 ± 0.95	67.8 ± 0.94
C_C (Counts/MeV/sec)	3.23 $\times 10^2$ ± 1.31	3.13 × 10^2 ± 1.39	3.05 × 10^2 ± 1.39
P/C	0.214 ± 0.004	0.248 ± 0.013	0.222 ± 0.0037

anticoincidence method.

4. Discussion

4.1. Feasibility analysis of the coincidence method in BNCT-SPECT system

Analytical results in section 3.2 demonstrated that appropriately handling crosstalk behavior using both the coincidence and the anti-coincidence methods significantly contributed to noise reduction. Moreover, the more the scintillator is arranged, the more frequently the crosstalk happens. So, further noise reduction can be expected in actual BNCT-SPECT. It is important to mention that these approaches are compatible and can be used concurrently. Traditionally, noise reduction has been attempted by only one of these methods. In contrast, the proposed method takes a novel approach by leveraging the crosstalk phenomenon to enhance the target signal, which is a key aspect of this study.

For the application of this approach to our BNCT-SPECT system (8 × 8 array-type GAGG scintillators), it is necessary to determine where the coincidence events happen in multiple detector elements. This information is involved in the feasibility of the coincidence method, and it was investigated through the dependency of the energy and angle of scattered photons based on the Compton Scattering effect. As a result of the Compton scattering interaction, a recoil electron and a scattered γ-ray are produced, and their energies are distributed depending on the scattering angle θ (Glenn, 2010). Therefore, considering the geometrical relationship between the two scintillators, the energy of the scattered photons can also be determined. Due to the thickness of the GAGG scintillator, the resulting energy takes a distribution, that indicates a characteristic shape for each scintillator.

To validate this hypothesis, a simulation system modeling the actual BNCT-SPECT configuration was developed. The crosstalk behavior at three points (A, B, C) was investigated by evaluating the deposited energy [T-deposit 2] according to the distance between scintillators. The simulation system is illustrated in Fig. 10, (a) shows the entire system, while (b) shows the positional relationship between the reference scintillator and the three evaluated scintillators (A, B, C). The reference scintillator is positioned directly below the mono-energetic 478 keV

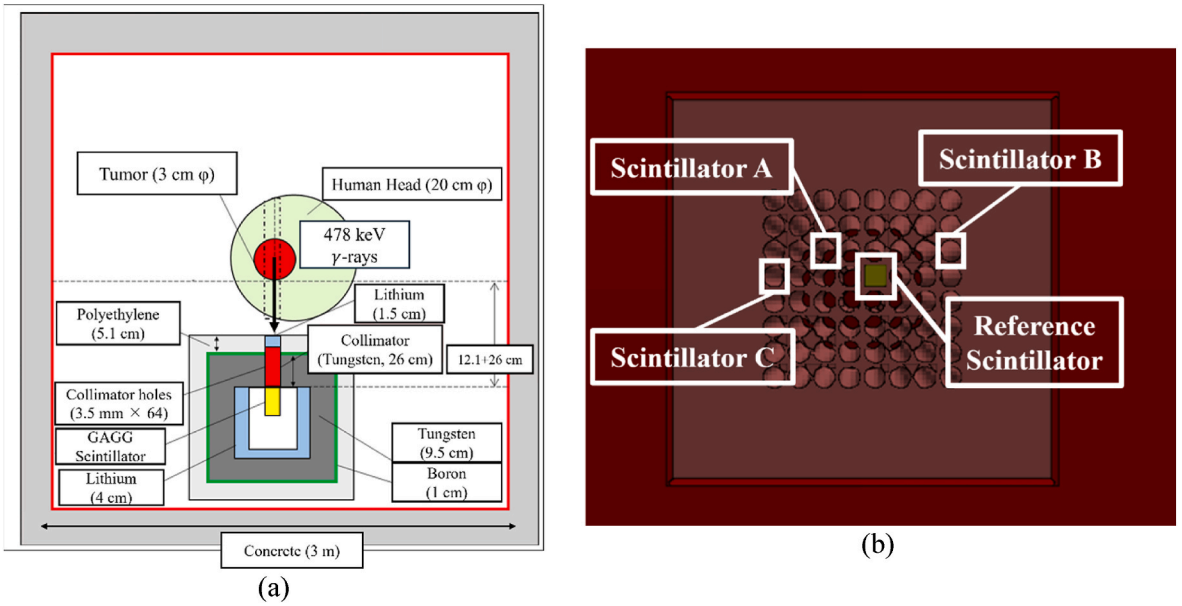

Fig. 10. The entire simulation system assuming clinical BNCT treatments, (b) GAGG scintillator arrangements. The reference scintillator is positioned directly below the 478 keV γ-rays source. Three scintillators were selected considering the symmetry of their arrangement, resulting in their concentration in the upper half. This γ-ray source is isotropic; however, source bias was set to irradiate γ-rays to the collimator.

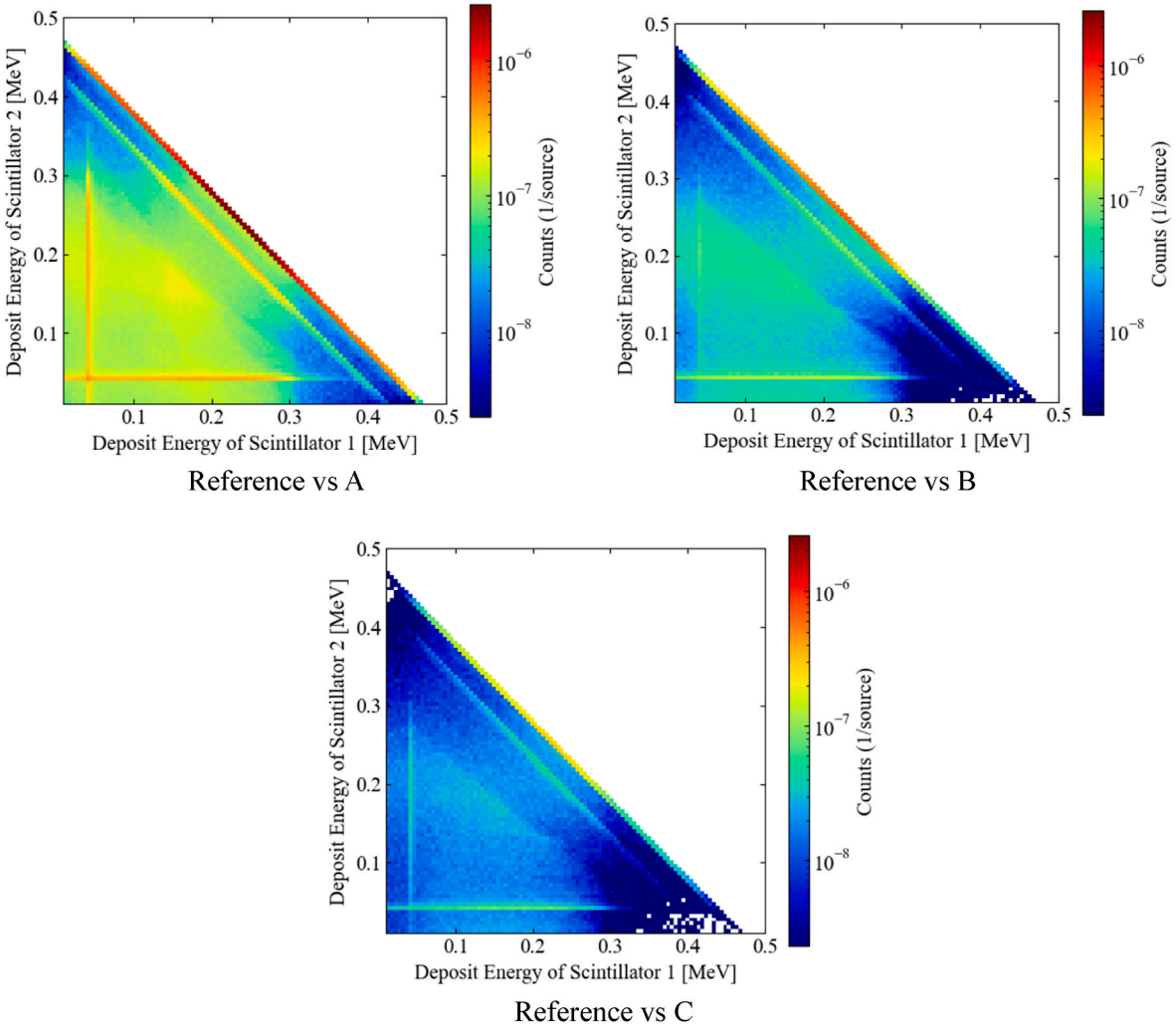

Fig. 11. Simulation results of [T-deposit 2] tally in the actual BNCT-SPECT system. The diagonal line shows the counts in the case that the sum of the deposited energy in each scintillator corresponds to 478 keV, $\boldsymbol{f_{(1+2)c}(478\,keV)}$. Three thick lines were observed in these results, and it was considered to the characteristic x-ray from Gadolinium (discussed in Section 4.2).

γ-ray source, that corresponds to the energy in the ^{10}B (n, α) ^{7}Li reaction, as introduced in Equation (1) and (2). The simulation results of coincidence events for each scintillator relative to the reference scintillator are presented in Fig. 11. The diagonal line shows the counts that the total of the deposited energy is equal to 478 keV ($f_{(1+2)c}(478\,keV)$). Three other thick lines were observed in each Figure, and it was considered characteristic X-ray from Gadolinium, as discussed in Section 4.2. Based on these simulation results, Fig. 12 shows the $f_{(1+2)c}(478\,keV)$ for the deposited energy to the reference scintillator in each case. The black dotted lines indicate the Compton edges between the reference and each scintillator. Thus, these results suggest that the contribution of scattered photons originating from the opposite scintillator diminishes with increasing distance between the scintillators. Moreover, the contribution of characteristic X-rays was also observed over the Compton edge, but these can be excluded from the target signals since their counts fall outside the energy ranges of the scattered photons. These findings demonstrate that the T-deposit 2 tally in PHITS enables detailed analyses of coincidence events.

However, this information is not sufficient for image reconstruction. When applying the coincidence method in BNCT-SPECT, it is crucial to determine which scintillator the photons enter first, i.e., which one absorbs the Compton electrons. According to Fig. 13, the energy deposition in the reference scintillator arises from both Compton electrons and scattered photons, corresponding to the region enclosed by the two black dotted lines. In the context of PET detectors, depth encoding PET detectors have been developed to improve parallax error, which can obtain the Depth-of-Interaction (DOI) information (Ito et al., 2011; Yamamoto et al., 2014; Zhao et al., 2024). DOI is also an important concept in this study. Without DOI information, we can just identify the deposited energy of this signal, and it is difficult to determine whether the coincidence counts originate from photoelectrons or from Compton electrons (see Fig. 13 (a)). As shown in Fig. 13 (b), we can also figure out the positional relationship between incident photons and scattered photons by analyzing the DOI with the deposited energy. Therefore, the origin of the coincidence counts can be determined.

4.2. Experimental limitation

Section 3 compared the experimental and simulated PHS results for the crosstalk phenomenon, showing that the simulation results were benchmarked against experiments and that PHITS can be effectively used for such analyses. However, several factors should be considered when interpreting the observed discrepancies. Fig. 7 shows that the experimental PHS of the S_1, directly irradiated by γ-rays, exhibits poorer energy resolution at the 662 keV peak compared to the calculation. This can be attributed to the small adhesive area of the GAGG scintillator and MPPC (3.5 × 3.5 mm^2), which made proper adhesion difficult. Therefore, light leakage from the scintillator during measurement led to a

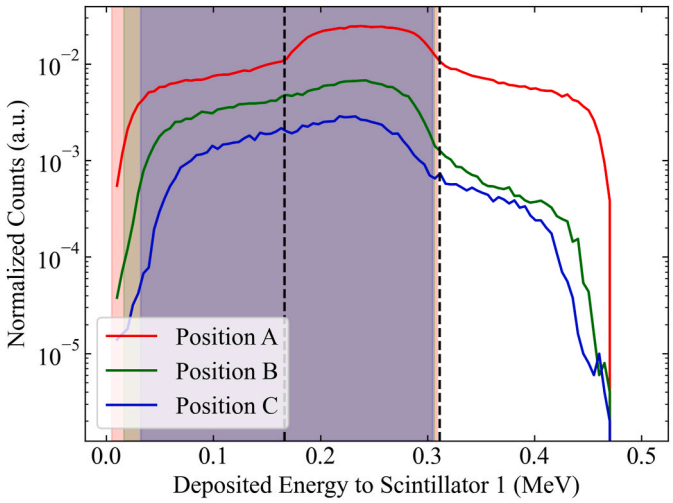

Fig. 12. Coincidence counts between the reference detector and each scintillator when the total deposited energy is 478 keV ($f_{(1+2)c}(478\,keV)$, extracted from the results in Fig. 11). All values are normalized corresponding to the maximum coincidence counts with scintillator A. The black dotted lines indicate the Compton edges between the reference and each scintillator. The colored regions represent the energy ranges corresponding to the scattering angle ranges determined by the geometrical configuration.

reduced count. Nevertheless, comparing the order of magnitude of the vertical axis between the experimental and calculated results indicates that the count rates are generally consistent. In contrast, the neighboring S_2 exhibits higher count rates in the experimental results than in the calculations across the entire energy range. This discrepancy can be attributed to noise present in the measurement environment due to the same adhesion issue between the GAGG scintillator and MPPC. Additionally, as the energy decreases, noise from physical causes related to the signal processing of the detector becomes more pronounced. It is important to reduce the noise inherent in such experimental environments.

As for the coincidence events (See Fig. 8), the experimental result in the coincidence events could almost reproduce the simulation results; however, the spectra of S_1 in the simulation show the escape peak around 618 keV. This is due to the photoelectric effect from Gadolinium, which emits 42.757 keV photons in this process (Hamaguchi et al., 2000). As the threshold was set higher than 42.757 keV, such photons weren't detected in this experiment. In addition, the complex electrical circuit system may affect the experimental results due to background noise.

Furthermore, this study focused on the accurate measurements of coincidence counts by the single source to demonstrate that the crosstalk phenomenon can improve the contribution of the background noise. However, it didn't represent the clinical situation in BNCT. As described in Section 1, there are several pathways for the background noise in BNCT treatments. Considering the radiation scattering effect, it is also important to perform experiments under the clinical environment, such as by implementing the water phantom. These works will contribute to advancing this approach for the precise real-time assessment of treatment effects in BNCT.

5. Conclusion

This study proposes the application of the crosstalk phenomenon to enhance the measurement accuracy of a real-time boron monitoring system in Boron Neutron Capture Therapy called BNCT-SPECT, which was experimentally validated. BNCT-SPECT aims to measure 478 keV γ-rays emitted from ^{10}B (n, α) ^{7}Li reactions; however, several background noises interrupt the measurement performance. Since our BNCT-SPECT system employs 8 × 8 array-type scintillators closely, the crosstalk phenomenon inevitably happens. By processing these signals properly in coincidence/anti-coincidence methods, it allows noise

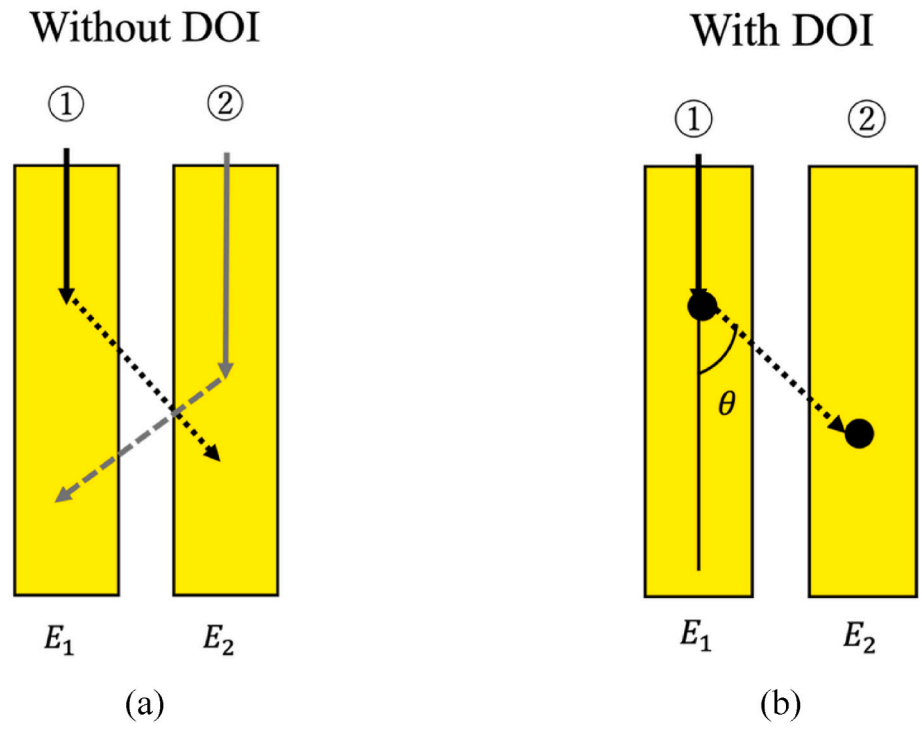

Fig. 13. Illustrations of coincidence events with/without DOI information. The solid line means incident photons, and the dotted line is scattered electrons. E_1 and E_2 are the deposited energies to each scintillator ① and ②. (a) Coincidence events without DOI information. Due to the wide range of scattering angles, both incidents cannot be distinguished. (b) Coincidence events with DOI information. The angle for the detected positions can be determined. If E_2 corresponds to the Compton scattered energy, the information on the incident particle can also be obtained.

reduction and increases counts for target signals.

We fabricated an experimental system with two GAGG scintillators based on a ^{137}Cs standard γ-ray source. The γ-ray energy spectra in each scintillator were obtained and compared with simulation results in PHITS. The results demonstrated good agreement, indicating that the analysis of the crosstalk phenomenon can be evaluated in PHITS. The performance of noise reduction in coincidence/anti-coincidence methods was assessed by the improvement rate of Peak-Compton ratio (P-C ratio, *R*), 15.9 % and 3.8 % for each method. In actual BNCT-SPECT, further noise reduction can be expected because the frequency of crosstalk should increase with the number of adjacent scintillators. However, identifying the target signals in the coincidence events is crucial, and the relationship regarding the scattering angle and the photon energy provides a useful means for this purpose. Analyses in [T-deposit 2] Tally of PHITS were performed for the actual BNCT-SPECT model to investigate the deposited energy between the distance of scintillators from the reference one. Simulation results could successfully reproduce the situation of the coincidence events and revealed that the effect of the scattering photons decreased as the distance the scintillators. Still, the discrimination of the target signal is difficult; however, the concept of DOI is considered promising to identify the target signals, which includes the next steps for the noise reduction in the coincidence method.

These findings serve as an important step for improving the monitoring performance of BNCT-SPECT using the crosstalk phenomenon. Also, we propose that the [T-deposit 2] tally in PHITS allows us to analyze the coincidence events for such purposes. Further research should include a detailed analysis of the coincidence events in the real environment of the BNCT-SPECT (8 × 8 array-type scintillators), and verification in the clinical BNCT situation.

CRediT authorship contribution statement

Yu Fujiwara: Writing – original draft, Visualization, Software, Investigation, Data curation. **Mana Miyagawa:** Validation, Investigation, Data curation, Conceptualization. **Mikito Yagura:** Validation, Methodology, Formal analysis, Data curation. **Jiye Qiu:** Writing – review & editing, Software. **Shingo Tamaki:** Resources, Methodology. **Sachie Kusaka:** Validation, Supervision, Resources. **Fuminobu Sato:** Writing – review & editing, Supervision, Resources, Project administration. **Isao Murata:** Writing – review & editing, Funding acquisition, Conceptualization.

Declaration of competing interest

The authors declare that they have no known competing financial interests or personal relationships that could have appeared to influence the work reported in this paper.

Data availability

Data will be made available on request.

References

Brown, J.M.C., 2023. Corrigendum to “In-Silico optimisation of tileable philips digital SiPM based thin monolithic scintillator detectors for SPECT applications” [Appl. Radiat. Isot. 168 109368 (2021)]. Appl. Radiat. Isot. 194, 110721. https://doi.org/10.1016/j.apradiso.2023.110721.

Caracciolo, A., Ferri, T., Borghi, G., Carminati, M., Protti, N., Altieri, S., Fiorini, C., 2024. A compact scintillator-based detector with collimator and shielding for dose monitoring in boron neutron capture therapy. Physics and Imaging in Radiation Oncology 29, 100556. https://doi.org/10.1016/j.phro.2024.100556.

Du, Y., Frey, E.C., 2009. Quantitative evaluation of simultaneous reconstruction with model-based crosstalk compensation for dual-isotope simultaneous acquisition brain SPECT. Med. Phys. 36 (6Part1), 2021–2033. https://doi.org/10.1118/1.3120411.

Glenn, F. Knoll, 2010. In: Radiation Detection and Measurement, fourth ed.

Glodo, J., Moses, W.W., Higgins, W.M., van Loef, E.V.D., Wong, P., Derenzo, S.E., Weber, M.J., Shah, K.S., 2005. Effects of Ce concentration on scintillation properties of LaBr/sub 3/:Ce. IEEE Trans. Nucl. Sci. 52 (5), 1805–1808. https://doi.org/10.1109/TNS.2005.856906.

Goorley, T., Nikjoo, H., 2000. Electron and photon spectra for three gadolinium-based cancer therapy approaches. Radiat. Res. 154 (5). https://doi.org/10.1667/0033-7587(2000)154[0556:EAPSFT]2.0.CO;2.

Hales, B., Katabuchi, T., Igashira, M., Terada, K., Hayashizaki, N., Kobayashi, T., 2017. Predicted performance of a PG-SPECT system using CZT primary detectors and secondary Compton-suppression anti-coincidence detectors under near-clinical settings for boron neutron capture therapy. Nucl. Instrum. Methods Phys. Res. Sect. A Accel. Spectrom. Detect. Assoc. Equip. 875. https://doi.org/10.1016/j.nima.2017.09.009.

Hamaguchi, K., Maeda, Y., Matsumoto, H., Nishiuchi, M., Tomida, H., Koyama, K., Awaki, H., Tsuru, T.G., 2000. X-ray CCD calibration system using fluorescent lines. Nucl. Instrum. Methods Phys. Res. Sect. A Accel. Spectrom. Detect. Assoc. Equip. 450 (2–3), 360–364. https://doi.org/10.1016/S0168-9002(00)00306-5.

International Atomic Energy Agency, 2023. Advances in Boron Neutron Capture Therapy.

Ishikawa, M., Kobayashi, T., Sakurai, Y., Kanda, K., 2001. Optimization technique for a prompt gamma-ray SPECT collimator system. J. Radiat. Res. 42 (4). https://doi.org/10.1269/jrr.42.387.

Ishiwata, K., 2019. 4-Borono-2-18F-fluoro-l-phenylalanine PET for boron neutron capture therapy-oriented diagnosis: overview of a quarter century of research. Ann. Nucl. Med. 33 (4), 223–236. https://doi.org/10.1007/s12149-019-01347-8.

Ito, M., Hong, S.J., Lee, J.S., 2011. Positron emission tomography (PET) detectors with depth-of- interaction (DOI) capability. Biomedical Engineering Letters 1 (2), 70–81. https://doi.org/10.1007/s13534-011-0019-6.

Kamada, K., Shoji, Y., Kochurikhin, V.V., Okumura, S., Yamamoto, S., Nagura, A., Yeom, J.Y., Kurosawa, S., Yokota, Y., Ohashi, Y., Nikl, M., Yoshikawa, A., 2016. Growth and scintillation properties of 3 in. diameter Ce doped Gd3Ga3Al2O12 scintillation single crystal. J. Cryst. Growth 452. https://doi.org/10.1016/j.jcrysgro.2016.04.037.

Kim, M., Hong, B.H., Cho, I., Park, C., Min, S.H., Hwang, W.T., Lee, W., Kim, K.M., 2021. Design of a scintillator-based prompt gamma camera for boron-neutron capture therapy: comparison of SrI2 and GAGG using Monte-Carlo simulation. Nucl. Eng. Technol. 53 (2). https://doi.org/10.1016/j.net.2020.07.010.

Kobayashi, T., Sakurai, Y., Ishikawa, M., 2000. A noninvasive dose estimation system for clinical BNCT based on PG-SPECT - conceptual study and fundamental experiments using HPGe and CdTE semiconductor detectors. Med. Phys. 27 (9). https://doi.org/10.1118/1.1288243.

Linko, S., Revitzer, H., Zilliacus, R., Kortesniemi, M., Kouri, M., Savolainen, S., 2008. Boron detection from blood samples by ICP-AES and ICP-MS during boron neutron capture therapy. Scand. J. Clin. Lab. Investig. 68 (8), 696–702. https://doi.org/10.1080/00365510802100831.

Locher, G.L., 1936. Biological effects and therapeutic possibilities of neutrons. Am. J. Roentgenol. Radium Ther. 36.

Manabe, M., Nakamura, S., Murata, I., 2016a. Study on measuring device arrangement of array-type CdTe detector for BNCT-SPECT. Rep. Practical Oncol. Radiother. 21 (2), 102–107. https://doi.org/10.1016/j.rpor.2015.04.002.

Manabe, M., Ohya, R., Saraue, N., Sato, F., Murata, I., 2016b. Cross talk experiment with two-element CdTe detector and collimator for BNCT-SPECT. Journal of Radiation Protection and Research 41 (4), 328–332. https://doi.org/10.14407/jrpr.2016.41.4.328.

Manabe, M., Sato, F., Murata, I., 2016c. Basic detection property of an array-type CdTe detector for BNCT–SPECT – measurement and analysis of anti-coincidence events. Appl. Radiat. Isot. 118. https://doi.org/10.1016/j.apradiso.2015.11.003.

Mao, R., Zhang, L., Zhu, R.-Y., 2008. Optical and scintillation properties of inorganic scintillators in high energy physics. IEEE Trans. Nucl. Sci. 55 (4), 2425–2431. https://doi.org/10.1109/TNS.2008.2000776.

Minami, K., Saraue, N., Ohya, R., Sato, F., Murata, I., 2017. Design of a proto-type array detector using GAGG scintillator for BNCT-SPECT. In: 9th Young Researchers’ BNCT Meeting (YBNCT 9).

Minsky, D.M., Valda, A.A., Kreiner, A.J., Green, S., Wojnecki, C., Ghani, Z., 2011. First tomographic image of neutron capture rate in a BNCT facility. Appl. Radiat. Isot. 69 (12), 1858–1861. https://doi.org/10.1016/j.apradiso.2011.01.030.

Miyamaru, H., Nguyen Quang, K., Le Viet, H., Kojima, T., 2025. Development of anticoincidence detector specializing in small-angle Compton scattering gamma rays for boron neutron capture therapy. Appl. Radiat. Isot. 217, 111646. https://doi.org/10.1016/j.apradiso.2024.111646.

Moszynski, M., Kapusta, M., Mayhugh, M., Wolski, D., Flyckt, S.O., 1997. Absolute light output of scintillators. IEEE Trans. Nucl. Sci. 44 (3), 1052–1061. https://doi.org/10.1109/23.603803.

Murata, I., Kusaka, S., Minami, K., Saraue, N., Tamaki, S., Kato, I., Sato, F., 2022. Design of SPECT for BNCT to measure local boron dose with GAGG scintillator. Appl. Radiat. Isot. 181. https://doi.org/10.1016/j.apradiso.2021.110056.

Murata, I., Nakamura, S., Manabe, M., Miyamaru, H., Kato, I., 2014. Characterization measurement of a thick CdTe detector for BNCT-SPECT - Detection efficiency and energy resolution. Appl. Radiat. Isot. 88. https://doi.org/10.1016/j.apradiso.2014.01.023.

Photonics, H., 2017. Multi-Pixel photon counters. https://Www.Hamamatsu.Com/Jp/En/Product/Optical-Sensors/Mppc/Mppc_mppc-Array/Index.Html. https://www.hamamatsu.com/jp/en/product/optical-sensors/mppc/mppc_mppc-array/index.html.

Qiu, J., Sakai, M., Voulgaris, N., Tamaki, S., Kusaka, S., Murata, I., 2025. Comprehensive design study of the Si/TlBr semiconductor-based Compton camera for 478 keV prompt gamma-ray imaging in boron neutron capture therapy. Jpn. J. Appl. Phys 64, 097001. https://doi.org/10.35848/1347-4065/ae02d5.

Rosado, J., Hidalgo, S., 2015. Characterization and modeling of crosstalk and afterpulsing in Hamamatsu silicon photomultipliers. J. Instrum. 10 (10). https://doi.org/10.1088/1748-0221/10/10/P10031. P10031–P10031.

Sakai, M., Parajuli, R.K., Kubota, Y., Kubo, N., Yamaguchi, M., Nagao, Y., Kawachi, N., Kikuchi, M., Arakawa, K., Tashiro, M., 2020. Crosstalk reduction using a dual energy window scatter correction in Compton Imaging. Sensors 20 (9), 2453. https://doi.org/10.3390/s20092453.

Sakai, M., Tamaki, S., Murata, I., Parajul, R.K., Matsumura, A., Kubo, N., Tashiro, M., 2023. Experimental study on Compton camera for boron neutron capture therapy applications. Sci. Rep. 13 (1). https://doi.org/10.1038/s41598-023-49955-9.

Sato, T., Iwamoto, Y., Hashimoto, S., Ogawa, T., Furuta, T., Abe, S.I., Kai, T., Matsuya, Y., Matsuda, N., Hirata, Y., Sekikawa, T., Yao, L., Tsai, P.E., Ratliff, H.N., Iwase, H., Sakaki, Y., Sugihara, K., Shigyo, N., Sihver, L., Niita, K., 2024. Recent improvements of the particle and heavy ion transport code system–PHITS version 3.33. J. Nucl. Sci. Technol. 61 (1). https://doi.org/10.1080/00223131.2023.2275736.

Sauerwein, W.A.G., Wittig, A., Moss, R., Nakagawa, Y., 2012. Neutron capture therapy: principles and applications. In: Neutron Capture Therapy: Principles and Applications, 9783642313349. https://doi.org/10.1007/978-3-642-31334-9.

Trigila, C., Kratochwil, N., Mehadji, B., Ariño-Estrada, G., Roncali, E., 2024. Intercrystal optical crosstalk in radiation detectors: monte carlo modeling and experimental validation. IEEE Transactions on Radiation and Plasma Medical Sciences 8 (7), 734–742. https://doi.org/10.1109/TRPMS.2024.3395131.

Tsartsalis, S., Tournier, B.B., Habiby, S., Ben Hamadi, M., Barca, C., Ginovart, N., Millet, P., 2018. Dual-radiotracer translational SPECT neuroimaging. Comparison of three methods for the simultaneous brain imaging of D2/3 and 5-HT2A receptors. Neuroimage 176, 528–540. https://doi.org/10.1016/j.neuroimage.2018.04.063.

Uenomachi, M., Shimazoe, K., Takahashi, H., 2022. Double photon coincidence crosstalk reduction method for multi-nuclide Compton imaging. J. Instrum. 17 (4), P04001. https://doi.org/10.1088/1748-0221/17/04/P04001.

Winkler, A., Koivunoro, H., Savolainen, S., 2017. Analysis of MCNP simulated gamma spectra of CdTe detectors for boron neutron capture therapy. Appl. Radiat. Isot. 124. https://doi.org/10.1016/j.apradiso.2017.03.018.

Yamamoto, S., Kobayashi, T., Yeol Yeom, J., Morishita, Y., Sato, H., Endo, T., Usuki, Y., Kamada, K., Yoshikawa, A., 2014. Development of GAGG depth-of-interaction (DOI) block detectors based on pulse shape analysis. Nucl. Instrum. Methods Phys. Res. Sect. A Accel. Spectrom. Detect. Assoc. Equip. 767, 289–295. https://doi.org/10.1016/j.nima.2014.09.001.

Zhao, B., Huang, Y., Wang, C., 2024. A continuous depth encoding PET detector using side readout of dual-layer GAGG crystals with SiPM array. Nucl. Instrum. Methods Phys. Res. Sect. A Accel. Spectrom. Detect. Assoc. Equip. 1059, 168975. https://doi.org/10.1016/j.nima.2023.168975.